Study of the lattice sites of Ti and Ni impurities in $LiNbO_3$ single crystals, by means of X-ray absorption spectroscopy

1991 J. Phys.: Condens. Matter 3 4135

(http://iopscience.iop.org/0953-8984/3/23/002)

J. Phys.: Condens. Matter 3 (1991) 4135–4144. Printed in the UK

Study of the lattice sites of Ti and Ni impurities in $LiNbO_3$ single crystals, by means of x-ray absorption spectroscopy

C Zaldo†, C Prieto†, H Dexpert‡ and P Fessler‡

† Instituto de Ciencia de Materiales de Madrid, Consejo Superior de Investigaciones Científicas, Campus Universitario de Cantoblanco (C-IV), 28049, Madrid, Spain

‡ Laboratoire pour l'Utilisation du Rayonnement Electromagnétique, Université de Paris Sud (Bâtiment 209D), 91405 Orsay, France

Received 3 January 1991, in final form 26 February 1991

Abstract. The structural environment of Ti and Ni ions incorporated into $LiNbO_3$ single crystals during the growing process has been studied by using x-ray absorption spectroscopies: extended x-ray absorption fine structure (EXAFS) and x-ray absorption near-edge structure (XANES) spectroscopies. It has been found that for the impurity concentration used (1% of TiO_2 and 0.1% NiO in the melt) both ions, Ti^{4+} and Ni^{2+}, are incorporated at the Li site of the $LiNbO_3$ lattice.

1. Introduction

$LiNbO_3$ is an important material because of its application in optoelectronics technology as an optical waveguide substrate [1], in photorefractive devices [2] and in solid state lasers as a host matrix [3].

In all of these applications the foreign ions in the material play a major role, because they are responsible for the modification of the optical properties of the matrix.

(i) Optical waveguides are created in $LiNbO_3$ by diffusing Ti at high temperature [1] or implanting Ti ions [4, 5] (Ti ions modify the refractive index of the substrate).

(ii) Photorefractive properties are introduced by doping the crystal with transition metal ions (mainly iron) [2].

(iii) Rare-earth ions (Nd and others) have been studied as possible impurities in producing solid state lasers [3].

In order to explain fully the optical modifications introduced by the impurities, their lattice location should be elucidated.

Early x-ray diffraction experiments [6] showed that Li ions are less strongly bonded to the lattice than Nb ones. This would suggest that Li ions would be easier to remove from the lattice than Nb ones. Recently, theoretical modelling of the impurities incorporated into $LiNbO_3$ [7] led to the conclusion that a self-compensating mechanism, i.e. simultaneous Li and Nb substitution, is the most favourable mechanism for the incorporation of impurities in $LiNbO_3$, if no other lattice defects are considered. Thus both Li and Nb sites would be expected to accommodate impurities.

0953-8984/91/234135 + 10 $03.50

The experimental determination of the lattice sites of impurities in $LiNbO_3$ had been, for a long time, seen as a very difficult task, because of the similarity of the first oxygen shells in Li and Nb sites, and a lot of experimental and theoretical work has been conducted in the past: pioneer spectroscopic experiments (electron paramagnetic resonance, EPR [8], and Mössbauer [9]) have indicated that the lattice locations of transition metal and rare-earth ions show trigonal symmetry. Nb and Li substitutional sites are possible, whereas the intrinsic vacancy was not generally considered, but conclusive evidence favouring a particular site was not obtained.

In the last two years the combined application of extended x-ray absorption fine-structure (EXAFS) spectroscopy, the Rutherford backscattering (RBS) channelling technique, perturbed angular correlation spectroscopy (PACS), proton-induced x-ray emission (PIXE) and electron–nuclear double-resonance (ENDOR) spectroscopy has helped to clarify the experimental situation: with the sole exception of Ta^{5+}, which has been found to replace niobium [10, 11], the extrinsic ions incorporated into the lattice in singly doped samples are accommodated on Li positions (Mn^{2+} [12, 13], Fe^{3+} [14], Eu^{3+} [11, 15, 16], Nd^{3+} [11, 16], Hf^{4+} [10, 11, 16, 17]), although Eu^{3+} and Nd^{3+} also exhibit considerable fractions on the Nb site, and Fe^{3+} a minor fraction.

The x-ray absorption near-edge structure (XANES) and EXAFS spectra of Ti introduced by diffusion into $LiNbO_3$ have been reported previously [18]. A distortion of the Ti environment in $LiNbO_3$ structure was found; however, no quantitative analysis of the EXAFS spectrum was provided and thus the uncertainty as regards the Ti site in the optical waveguide area remains.

It is commonly assumed [19] that Ti diffusion in $LiNbO_3$ takes place via the niobium vacancies present in the congruent material; according to this model the site for Ti would be the Nb site. Indeed, this result has been found for Ti-implanted $LiNbO_3$ [4] after a thermal recrystallization of the surface of the sample.

The diversity of experimental methods used for the incorporation of Ti in the lattice and the inhomogeneity of the Ti concentration inherent to the surface-incorporation processes make it useful to make a comparison with the situation when the Ti is more homogeneously incorporated during the crystal growth.

In this work, we have analysed the information provided by EXAFS measurements on single crystals in order to determine the lattice positions of Ti and Ni impurities introduced during the growth. It is necessary to use the EXAFS fluorescence technique mainly because of the large x-ray absorbing cross section of the Nb in the matrix. The spectra obtained are noisy due to the relatively low impurity concentration. This limits the accuracy of the determination of the atomic distances and coordination numbers. However, the analysis of the spectra can provide unambiguous evidence that the Li site should be selected for both Ti^{4+} and Ni^{2+} impurities.

2. Experimental techniques

Congruent $LiNbO_3$ single crystals have been grown by the Czochralski method. 1% of TiO_2 and 0.1% of NiO were added to the melt. The Ti and Ni molar concentrations in the crystal have been estimated to be 0.8% and 0.05%, respectively, as derived from the segregation coefficient reported for both ions [20]. The samples were plates cut with their large faces perpendicular to the *c*-axis. This axis was placed in the horizontal plane of the machine and tilted by about 45° with respect to the x-ray beam. Bragg diffractions

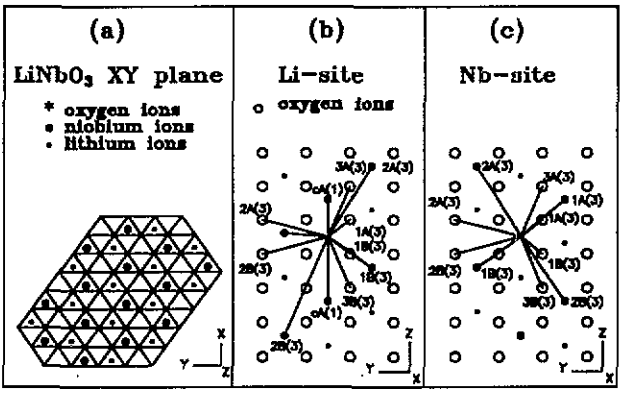

Figure 1. Room temperature $LiNbO_3$ structure. The sublattice of oxygens is considered regular for the sake of simplicity. (*a*) Projection on the *XY* plane. (*b*) Atomic distribution around the Li site. (*c*) Atomic distribution around the Nb site. In (*b*) and (*c*) the plane of oxygens is closer to the observer than the Li or Nb ions. The first digit in the notation stands for the order of the shell; ions along the *c*-axis are denoted as c; A and B denote ions belonging to the plane above (A) or below (B) the centre; the lack of a letter means that the ions and the centre belong to the same plane; finally, the number in the brackets stands for the number of equivalent ions.

were avoided by spatially shielding the detector window. Even so, at high x-ray energies (the Ni case) small Bragg diffractions appear in the spectrum; the part of the spectrum affected has been removed (see figure 4(*b*)).

Fluorescence spectra were acquired at room temperature (RT) at the K edges of Ti and Ni. We used synchrotron radiation emitted by the LURE (Orsay) DCI storage ring, running at 1.85 GeV, at the EXAFS-IV beam station, with an average current of 250 mA. X-rays were monochromatized using a Si(311) two-crystal spectrometer. The fluorescence was detected using a plastic scintillator attached to a photomultiplier [21].

3. $LiNbO_3$ structure

The $LiNbO_3$ structure has been determined by x-ray and neutron diffraction [6, 22, 23]. The structure is made up of irregular oxygen octahedra piled along the ferroelectric *c*-axis and sharing faces. The centres of the octahedra are occupied by cations in the sequence Li^+, Nb^{5+} and a vacancy octahedron. Furthermore, both Li^+ and Nb^{5+} are displaced (in opposite senses) along the c-axis towards the neighbouring vacancies.

Figure 1 provides a picture of the structure of an *XY* plane of the $LiNbO_3$ lattice as well as the notation used for the different neighbours considered to discuss the EXAFS results reported later.

The radial distances of the atoms neighbouring the oxygen octahedron centre are depicted in figure 2(*a*) and (*b*) for Li and Nb positions respectively. The distances are given as functions of the displacement, δ, from the point of the *c*-axis equidistant from the upper and lower faces of the oxygen octahedron (see figure 1). The displacement, δ, is considered positive in the positive direction of the ferroelectric *c*-axis (i.e. in the lithium–niobium–vacancy direction along the axis).

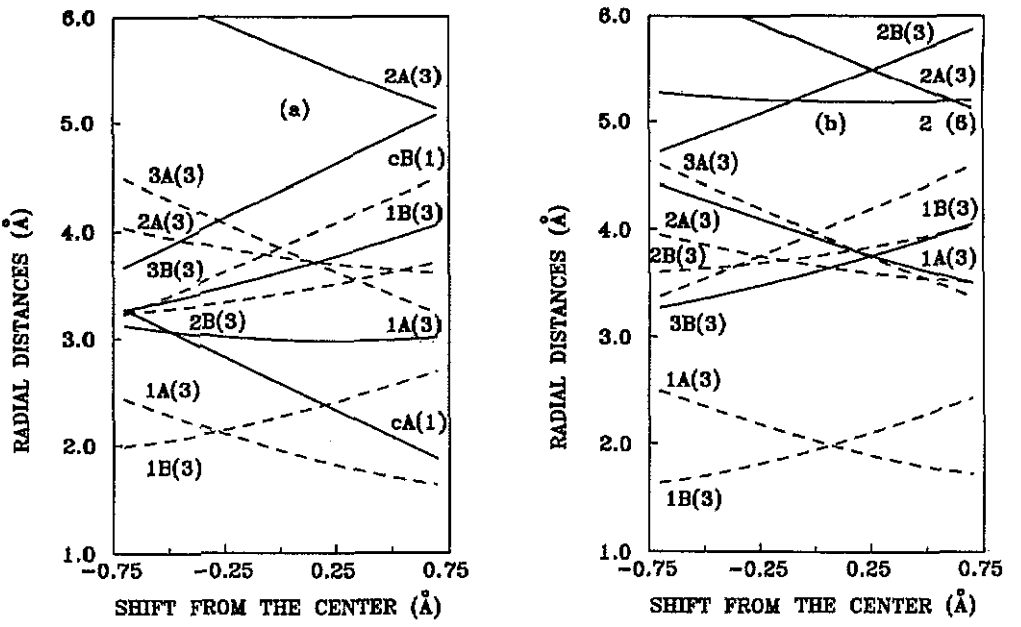

Figure 2. Impurity–host-ion radial distances calculated for oxygen (broken curve) and niobium (full curve) in the $LiNbO_3$ lattice as a function of the displacement, δ, from the centre of the octahedron. δ is considered positive in the positive direction of the c-axis. The centre is considered as the point of the c-axis equidistant from the two oxygen planes that form the first shell. Labels on the left-hand side refer to oxygen distances and on the right-hand one to niobium distances. (*a*) Li site. (*b*) Nb site.

Li ions are not included in figure 2 because their contribution to the EXAFS signal is minor due to the low backscattering amplitude of Li ($Z = 3$). On the other hand, a vacancy site will not be considered because RBS and PIXE experiments [11, 14–17] have shown that the vacancy site is free of impurities in all the singly doped cases studied, in accordance with theoretical expectations [7].

4. Experimental results, data analysis and discussion

4.1. X-ray absorption in the K edge region

Figure 3 shows the x-ray absorption of the doped $LiNbO_3$ samples in the region near to the absorption edge of the impurities. Also, the spectra corresponding to the reference compounds used are given for comparison purposes.

The spectra reported in figure 3(*a*) show the x-ray absorption of Ti^{4+} in $SrTiO_3$ single crystal and in powdered rutile (TiO_2), together with the spectrum corresponding to $LiNbO_3$. The shape of the x-ray absorption spectrum for Ti^{4+} is very sensitive to the lack of O_h symmetry [24, 25]. The characteristic features of the Ti^{4+} x-ray absorption can be observed for both the reference compounds ($SrTiO_3$, TiO_2) and the compound under investigation ($LiNbO_3$:Ti); however, the intensity of each peak is strongly dependent on the particular Ti environment. Following the usual notation [25], three peaks, denoted A_1, A_2 and A_3, present in the region 4960–4970 eV, have been respectively

attributed to a Frenkel exciton and to the $1s^1 \rightarrow t_{2g}$ and e_g electronic transitions. At higher energies other features appear in the spectra denoted as B (≃4975 eV), C_1 (≃ 4978 eV) and C_2 (≃4983 eV) (C_1 and C_2 peaks are associated with $1s^1 \rightarrow 4s$ and 4p electronic transitions, respectively); and, finally, two broader peaks D_1 (≃4990 eV) and D_2 (≃5002 eV) are also present. This indicates that, in the $LiNbO_3$ sample we used, the Ti was for the most part in the form of Ti^{4+}. In fact, our sample did not present any of the optical features associated with the presence of Ti^{3+} [26].

The spectrum of Ti in $LiNbO_3$ shown in figure 3(*a*) is closer to that obtained for rutile (where two Ti–O distances are present [27]) than to that obtained for $SrTiO_3$ (where Ti^{4+} is surrounded by very regular oxygen octahedra [28]). This seems to indicate that the oxygen octahedron around Ti in $LiNbO_3$ is distorted, as is the case for rutile; this is indeed consistent with what is expected from the $LiNbO_3$ lattice structure.

Finally Ni in $LiNbO_3$ is normally present as Ni^{2+}, as deduced from the EPR and optical spectroscopy studies [29, 30]—the thermal history of the sample thus does not modify the Ni oxidation state (low-temperature γ-irradiation is needed to induce other oxidation states [31]). The comparison shown in figure 3(*b*) between the Ni-doped $LiNbO_3$ and NiO powder, and the comparison of the second derivatives of the spectra of figure 3(*b*) support the conclusion that Ni^{2+} is the ion present in our sample.

4.2. EXAFS of Ti-doped $LiNbO_3$ single crystals

Figure 4(*a*) shows the x-ray fluorescence spectrum, $\mu(E)$, of the Ti-doped $LiNbO_3$. A classical procedure has been used to analyse the EXAFS spectrum: above the edge, the signal background is removed by a multi-iteration curve-smoothing procedure.

The analysis of the EXAFS signal to obtain the position of the neighbours around the impurity has been carried out using the well known EXAFS expression [32]

$$\chi(k) = \sum_j \frac{N_j}{kR_j^2} \exp(-2k^2\sigma_j^2) \exp(-\Gamma_j R_j/k) f_j(k) \sin(2kR_j + \varphi_j(k)). \tag{1}$$

This expression describes the EXAFS oscillations for a Gaussian distribution of neighbours around the central atom, in the single-scattering theory and in the plane-wave approximation. k is the wave vector of the photoelectron, which is related to the electron mass (m_e) and the threshold energy (E_0) by

$$k = [(2m_e/\hbar^2)(E - E_0)]^{1/2}. \tag{2}$$

N_j is the average coordination number for the Gaussian distribution of distances centred at the R_j-value, σ_j is the Debye–Waller contribution, $\varphi_j = 2d + Y_j(k)$ is the phase shift, d and Y_j being the central and backscattering atom phase shifts respectively, $f_j(k)$ is the amplitude of the backscattering atoms and Γ_j is related to the mean free path of the photoelectron.

Figure 5(*a*) shows the Fourier transform of the $k^3\chi(k)$-weighted signal (hereafter we refer to this function as the PRDF). The peaks that appear in this function have to be corrected by the $\varphi_j(k)$ contribution to obtain the 'true' distances of the defect.

Figure 5(*a*) shows two main peaks at about 1.46 and 2.84 Å (denoted I and II respectively) which are to be related to the oxygen and niobium neighbours. The presence of those peaks has been found essentially independently of the Fourier transform procedure, and most of the information of the EXAFS spectrum is included in them, since the back Fourier transform of the PRDF function in the limited range 1.3–3.9 Å approximately reproduces the EXAFS oscillations.

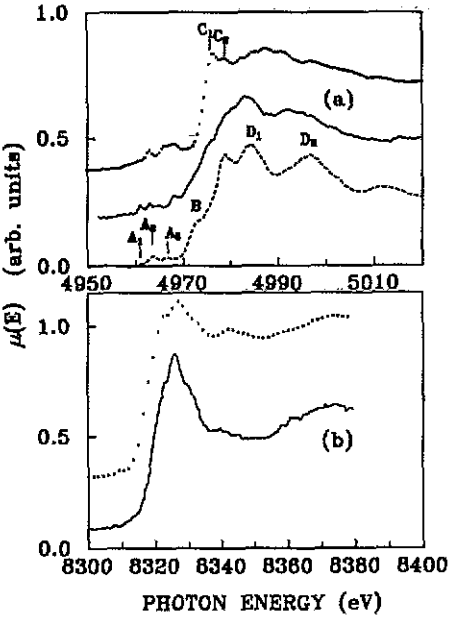

Figure 3. XANES spectra of doped $LiNbO_3$ single crystals and reference compounds. (*a*) $SrTiO_3$ single crystals (points); $LiNbO_3$:Ti single crystal (full trace); powdered rutile, TiO_2 (broken trace). (*b*) As-grown $LiNbO_3$:Ni single crystal (full trace); powdered NiO (points).

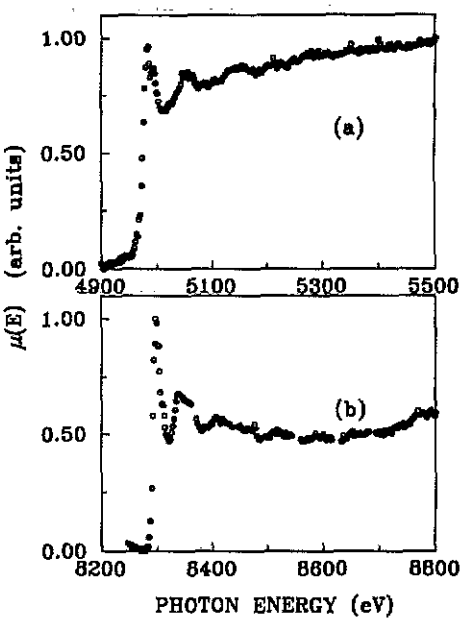

Figure 4. Room temperature fluorescence yield $\mu(E)$ of doped $LiNbO_3$ single crystals, measured at the K edge of the impurity. (*a*) 1% Ti-doped sample. (*b*) 0.1% Ni-doped sample.

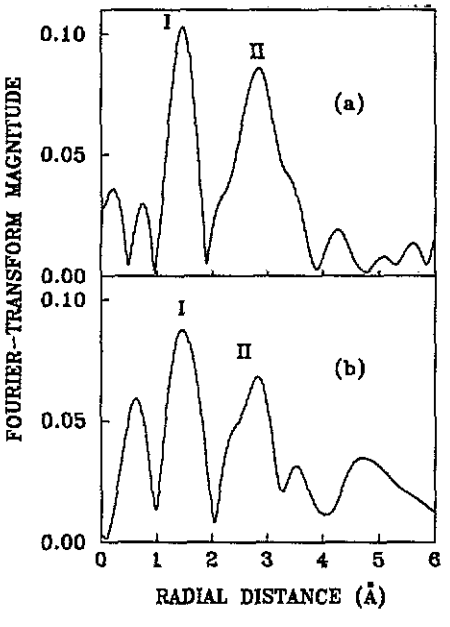

Figure 5. Fourier transform magnitude (PRDF) of the $k^3\chi(k)$-weighted EXAFS signal of doped $LiNbO_3$ single crystals. A Hanning window was used for apodization. (*a*) 1% Ti-doped sample; limits of the window: 25, 40–350, 500 eV. (*b*) 0.1% Ni-doped sample; limits of the window: 23, 33–250, 350 eV.

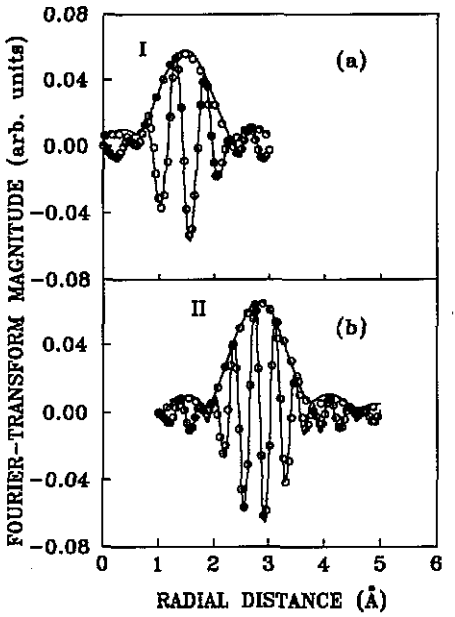

Figure 6. $LiNbO_3$:Ti. Distance-space comparison between the calculated PRDF (full curve) and the experimental filtered data (circles) of the modulus and imaginary part of the Fourier transform for the two significant peaks of figure 5(*a*). (*a*) Peak I; filter range of the back Fourier transform of the experimental data: 1.0–2.0 Å. (*b*) Peak II; filter range of the back Fourier transform of the experimental data: 2.2–3.8 Å.

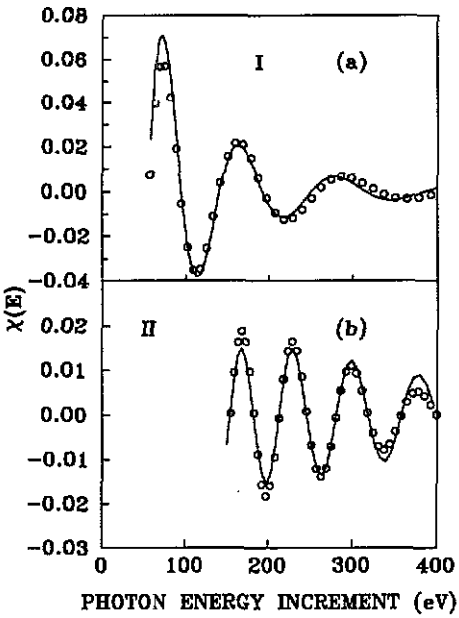

Figure 7. $LiNbO_3$:Ti. Energy-space comparison between the calculated EXAFS signal (full curve) and the experimental filtered data (circles) for the two significant peaks of figure 5(*a*). (*a*) Peak I; filter range of the back Fourier transform of the experimental data: 1.0–2.0 Å. (*b*) Peak II; filter range of the back Fourier transform of the experimental data: 2.2–3.8 Å.

The appearance of the PRDF spectra shown in figure 5(*a*) is similar to that reported previously for Mn [12] and Hf [10] impurities in $LiNbO_3$. Those two impurities have been found to be accommodated at the Li site. The first peak of the PRDF function (appearing in all cases at about 1.5 Å) has been associated with the presence of the six lattice oxygens in the first shell, and the second one with the combined effect of three niobiums above the plane of the impurity with three others below it.

This similarity suggests that the Ti incorporated into the $LiNbO_3$ lattice during growth lies at the Li site.

To obtain an accurate determination of the crystallographic distances, and thus a confirmation of the above hypothesis, we have minimized (using a standard minimization procedure) the difference between the experimental filtered data and the function $\chi(k)$ calculated according to expression (1) using the corresponding amplitudes and phases reported by McKale *et al* [33]. In the refinements the coordination number was fixed according to those corresponding to the expected Li site: $N_j = 6$ for both oxygen and niobium shells. Additionally, we have used the EXAFS spectrum of $SrTiO_3$ single crystal as a reference compound to provide initial values for the Debye–Waller (σ_j) and electron free path (Γ_j) parameters.

Figures 6 and 7 show the comparison, in distance and energy spaces respectively, of the experimental data and the calculated data for the atomic radial distribution and $\chi(E)$

Table 1. The set of values used in the best fit of the reference compounds and the compounds investigated. N_j is the number of neighbours, R_j is the mean distance, σ_j is the Debye–Waller factor, Γ_j is related to the electron mean free path and ΔE_0 is introduced to compensate for experimental errors between the spectra of $LiNbO_3$ samples and the experimental or theoretical references. Values marked with asterisks have been taken from x-ray diffraction experiments on $SrTiO_3$ [28] and $Ni(NO_3)_2 \cdot 6H_2O$ [34].

Sample	Peak (pair)	N_j	R_j (Å)	σ_j (Å)	Γ_j (Å^{-2})	ΔE_0 (eV)
$SrTiO_3$	I (Ti–O)	6*	1.953*	0.086	2.90	7
$LiNbO_3$:Ti	I (Ti–O)	6	1.97 ± 0.05	0.080	1.90	0
	II (Ti–Nb)	6	3.18 ± 0.05	0.070	1.80	−5
$Ni(NO_3)_2$:$6H_2O$	I (Ni–O)	6*	2.050*	0.091	1.80	1.5
$LiNbO_3$:Ni	I (Ni–O)	6	2.01 ± 0.05	0.078	1.80	−2
	II (Ni–Nb)	6	3.10 ± 0.05	0.092	1.82	1

functions. The best fit is obtained for the set of values of R_j, σ_j, Γ_j and ΔE_0 summarized in table 1.

The fairly good agreement shown in figures 6 and 7 confirms that Ti ions are surrounded by six oxygens at a mean distance of 1.97 ± 0.05 Å and by six niobiums at a mean distance of 3.18 ± 0.05 Å as reported in table 1. This placement is in good agreement with that expected for Ti, being in the centre of the oxygen octahedron corresponding to the Li site (see figure 2(*a*)). In this case, considering the rigid lattice of $LiNbO_3$ [6, 22, 23], there would be six oxygens at a mean distance of 2.1 Å and six niobiums at a mean distance of 3.3 Å.

Siting at the Nb site cannot account for the distances reported in table 1 because the six niobiums closer to the centre of the oxygen octahedron are at a mean distance of 3.8 Å (see figure 2(*b*)), which is too far from the distance found experimentally.

4.3. EXAFS of Ni-doped $LiNbO_3$ single crystals

The results of the analysis of the EXAFS spectrum of Ni^{2+} in $LiNbO_3$ (reported in figure 4(*b*)) are rather similar to those for analysis of the Ti one. Figure 5(*b*) shows the Fourier transform of the EXAFS signal after removal of the x-ray absorption background. Again, two main peaks are observed, marked as I and II.

To provide the initial values of σ_j and Γ_j for the fitting of peak I, we have used as a reference the compound $Ni(NO_3)_2 \cdot 6H_2O$, where the first shell of neighbours of Ni is formed by a nearly regular octahedron of oxygens at a mean distance 2.050 Å [34]. The values of σ_j and Γ_j obtained after fitting the reference compound with the McKale phases have been transferred to the fitting of the EXAFS spectrum of Ni in $LiNbO_3$.

Following a parallel procedure to that performed above for Ti, peak I has been fitted using the McKale phases and amplitudes, assuming that it corresponds to the presence of six oxygens, and taking as initial values for the fiting process the values of σ_j and Γ_j obtained in the reference compound. Peak II has been directly fitted with the McKale phases and amplitudes corresponding to niobium and it has been found to be consistent with the assumption of six niobiums at the second shell (the fittings, similar to those shown in figures 6 and 7, are not shown for the sake of brevity). The true distances R_j, and the set of values of σ_j, Γ_j and ΔE_0 obtained for the best fit have been summarized in table 1.

From the comparison between the Ni–Nb distance (3.10 Å) found in $LiNbO_3$ and those reported in figure 2, it has to be concluded that Ni^{2+} is also mainly replacing Li ions of the $LiNbO_3$ lattice, as in the Ti case above.

5. Further comments on the lattice sites of the impurities in $LiNbO_3$ single crystals

According to our present knowledge of the experimental results on the lattice sites of impurities in $LiNbO_3$ ([10–17], this work), the impurities that do not strongly distort the $LiNbO_3$ lattice (with ionic radii <1 Å), enter mainly at the lithium site of the lattice for doping levels between about 0.1 and 1%. The only exception to this rule is for the Ta^{5+}, which are accommodated in the regular Nb^{5+} site [10] and consequently do not need charge compensation.

This is somewhat surprising in view of the conclusion from theoretical modelling [7], which predicts a self-compensating mechanism to accommodate the charge misfit between the impurity and the replaced lattice cations. Thus both Li and Nb sites would be present with relative concentrations depending on the impurity charge.

Mg [35] and Zn [36] impurities in $LiNbO_3$ have a strong influence on the material properties. The impurity-related changes are functions of the impurity concentration up to a threshold of about 6%. To explain this behaviour it has been suggested [35] that Mg ions replace the antisite niobiums (niobiums in lithium sites) present in the congruent compound $LiNbO_3$ [37]; thus, below the impurity concentration threshold, the lattice site of Mg would be the Li site. The experimental results mentioned above may indicate that this could also be the mechanism controlling the incorporation of most of the impurities in $LiNbO_3$. Thus, impurities could be found in niobium sites (the theoretical expectation) only when locally the antisite niobiums have been removed, because the local impurity concentration is above the threshold (6%) or because of a local departure from the congruency of the crystal that decreases this threshold.

In fact, for Ti-diffused optical waveguides, a change in the symmetry of the Ti centre has been found when the mean Ti concentration is above 1.3% (5×10^{20} atoms cm^{-3}) [18]. This may indicate that a concentration threshold is also present for the Ti case.

More experimental work is needed to confirm the above suggestion, and future work should be addressed to studying the lattice location of the impurities in $LiNbO_3$ as related to the impurity concentration.

6. Conclusions

In conclusion, we have found that, for the impurity concentration used, Ti^{4+} and Ni^{2+} ions in $LiNbO_3$ are in general accommodated at the Li site. However, the possibility a minor fraction of both impurities being accommodated at other lattice sites cannot be excluded.

Acknowledgments

The Spanish authors are indebted to LURE for the assistance and experimental facilities provided, and thank Dr L Arizmendi and Dr E Diéguez for the provision of the samples. This work has been supported by CICyT (project MAT88-0431-C02).

References

[1] Armenise M N, Canali C, de Sario M and Zanoni E 1983 *Mater. Chem. Phys.* **9** 267
[2] Krätzig E and Schirmer O F 1988 *Photorefractive Materials and their Applications I (Springer Topics in Applied Physics 61)* (Berlin: Springer) ch 5
[3] Johnson L F and Ballman A A 1969 *J. Appl. Phys.* **40** 297
[4] Buhal Ch, Mantl S and Thomas D K 1987 *Proc. Fundamentals of Beam–Solids Interactions and Transient Thermal Processing Symp. (Pittsburg, PA, 1987)* p 317
[5] Poker D B and Thomas D K 1989 *J. Mater. Res.* **4** 412
[6] Abrahams S C, Reddy J M and Bernstein J L 1966 *J. Phys. Chem. Solids* **27** 997
[7] Donnerberg H J, Tomlinson S M and Catlow C R 1991 *J. Phys. Chem. Solids* **52** 201
[8] Halliburton L E 1989 *Properties of Lithium Niobate (EMIS Data Reviews Series 5)* (New York: EMIS) ch 6.4
[9] Keune W, Date S K, Dézsi I and Gonser U 1975 *J. Appl. Phys.* **46** 3914
[10] Prieto C, Zaldo C, Fessler P, Dexpert H, Sanz-García J A and Diéguez E 1991 *Phys. Rev.* B **43** 2594
[11] Rebouta L, Soares J C, da Silva M F, Sanz García J A, Diéguez E and Agulló-López F 1991 to be published
[12] Zaldo C, Agulló-López F, García J, Marcelli A and Mobilio S 1989 *Solid State Commun.* **71** 243
[13] Corradi G, Söthe H, Spaeth J M and Polgár K 1990 *J. Phys.: Condens. Matter* **2** 6603
[14] Rebouta L, da Silva M F, Soares J C, Hage-Ali M, Stockert J P, Siffert P, Sanz García J A, Diéguez E and Agulló López F 1991 *Europhys. Lett.* at press
[15] Rebouta L, Soares J C, da Silva M F, Sanz-García J A, Diéguez E and Agulló-López F 1989 *Appl. Phys. Lett.* **55** 120
[16] Rebouta L, Soares J C, da Silva M F, Sanz-García J A, Diéguez E and Agulló-López F 1990 *Nucl. Instrum. Methods Phys. Res.* B **50** 428
[17] Rebouta L, Soares J C, da Silva M F, Sanz-García J A, Diéguez E and Agulló-López F 1990 *Nucl. Instrum. Methods Phys. Res.* B **45** 495
[18] Skeath P, Elam W T, Burns W K, Stevie F A and Briggs T H 1987 *Phys. Rev. Lett.* **59** 1950
[19] Twingg M E, Maher D M, Nakahara S, Sheng T T and Holmes R J 1987 *Appl. Phys. Lett.* **50** 501
[20] Räuber A 1978 *Current Topics in Materials Science* vol 1 ed E Kaldis (Amsterdam: North-Holland) p 481
[21] Tourillon G, Guay D, Lemonnier M, Bartol F and Badeyan M 1990 *Nucl. Instrum. Methods Phys. Res.* A **294** 382
[22] Shiozaki Y and Mitsui T 1963 *J. Phys. Chem. Solids* **24** 1057
[23] Abrahams S C, Hamilton W C and Reddy J M 1966 *J. Phys. Chem. Solids* **27** 1013
[24] Waychunas G A 1986 *J. Physique Coll.* **47** C8 841
[25] Poumelec B, Marucco J F and Touzelin B 1986 *Phys. Status Solidi* b **137** 519
[26] Sanz García J A, Diéguez E, López F J and Agulló López F 1989 *Solid State Commun.* **72** 1159
[27] Abrahams S C and Bernstein J L 1971 *J. Chem. Phys.* **55** 3206
[28] Cowley R A 1984 *Phys. Rev.* A **134** 981
[29] Quan X, Guiru B and Minguang Z 1987 *Ferroelectrics* **76** 233
[30] Arizmendi L, Cabrera J M and Agulló F 1984 *Ferroelectrics* **56** 79
[31] Korradi G, Polgár K, Bugai SA A, Zaritskii I M, Rakitina L G, Grachev V G and Deryugina N I 1986 *Sov. Phys.–Solid State* **28** 412
[32] Teo B K 1986 *EXAFS: Basic Principles and Data Analysis (Springer Inorganic Chemistry Concepts 9)* (Berlin: Springer) ch 2
[33] McKale A G, Veal B W, Paulikas A P, Chan S K and Knapp G S 1988 *J. Am. Chem. Soc.* **110** 3763
[34] Bigoli F, Braibanti A, Tiripicchio A and Tiripicchio Camellini M 1971 *Acta Crystallogr.* B **27** 1427
[35] Schirmer O F, Thiemann O and Wöhlecke M 1991 *J. Phys. Chem. Solids* **52** 185
[36] Volk T R, Pryalkin, V I and Rubinina N M 1990 *Opt. Lett.* **15** 996
[37] Abrahams S C and Marsch P 1986 *Acta Crystallogr.* B **42** 61